Acta Crystallographica Section D
Biological Crystallography
ISSN 0907-4449

High-resolution structure of human D-glyceraldehyde-3-phosphate dehydrogenase

Jermaine L. Jenkins and John J. Tanner*

Departments of Chemistry and Biochemistry, University of Missouri-Columbia, USA

Correspondence e-mail: tannerjj@missouri.edu

Received 7 October 2005
Accepted 16 December 2005

PDB Reference: GADPH, 1u8f, r1u8fsf.

GAPDH (D-glyceraldehyde-3-phosphate dehydrogenase) is a multifunctional protein that is a target for the design of antitrypanosomatid and anti-apoptosis drugs. Here, the first high-resolution (1.75 Å) structure of a human GAPDH is reported. The structure shows that the intersubunit selectivity cleft that has been leveraged in the design of antitrypanosomatid compounds is closed in human GAPDH. Modeling of an anti-trypanosomatid GAPDH inhibitor in the human GAPDH active site provides insights into the basis for the observed selectivity of this class of inhibitor. Moreover, the high-resolution data reveal a new feature of the cleft: water-mediated intersubunit hydrogen bonds that assist closure of the cleft in the human enzyme. The structure is used in a computational ligand-docking study of the small-molecule compound CGP-3466, which inhibits apoptosis by preventing nuclear accumulation of GAPDH. Plausible binding sites are identified in the adenosine pocket of the NAD^+-binding site and in a hydrophobic channel located in the center of the tetramer near the intersection of the three molecular twofold axes. The structure is also used to build a qualitative model of the complex between GAPDH and the E3 ubiquitin ligase Siah1. The model suggests that the convex surface near GAPDH Lys227 interacts with a large shallow groove of the Siah1 dimer. These results are discussed in the context of the recently discovered NO–*S*-nitrosylation–GAPDH–Siah1 apoptosis cascade.

1. Introduction

GAPDH is an NAD^+-dependent glycolytic enzyme that catalyzes the formation of 1,3-bisphosphoglycerate from glyceraldehyde-3-phosphate and inorganic phosphate. The enzyme is ubiquitous in nature and cellularly abundant, which has led to widespread study of its function, structure and roles in human health and disease. For example, GAPDH is an attractive target for the design of drugs to combat protozoan parasites whose bloodstream forms depend solely on glycolysis for energy production (Sherman, 1998; de Marchi *et al.*, 2004; Ladame *et al.*, 2003; Leitao *et al.*, 2004; Menezes *et al.*, 2003; Kim *et al.*, 1995; Callens & Hannaert, 1995; Kim & Hol, 1998; Aronov *et al.*, 1998, 1999; Verlinde *et al.*, 1994; Bressi *et al.*, 2001; Suresh *et al.*, 2001). Enzymes that have been targeted for drug design include GAPDHs from the trypanosomatid species *Leishmania mexicana*, *Trypanosoma cruzi* and *T. brucei*, which are responsible for the debilitating illnesses leishmaniasis, Chagas disease and African sleeping sickness, respectively (Aronov *et al.*, 1998, 1999; Bressi *et al.*, 2001; de Marchi *et al.*, 2004; Ladame *et al.*, 2003; Leitao *et al.*, 2004;

Menezes *et al.*, 2003). Inhibitors of GAPDH from *Plasmodium falciparum* have also been proposed in the fight against malaria (Daubenberger *et al.*, 2000). As part of this effort, the crystal structures of GAPDHs from *L. mexicana* (Kim *et al.*, 1995; Suresh *et al.*, 2001; Aronov *et al.*, 1999), *T. cruzi* (Castilho *et al.*, 2003; Ladame *et al.*, 2003), *T. brucei* (Vellieux *et al.*, 1993) and *P. falciparum* (Satchell *et al.*, 2005) have been determined to aid structure-based drug design.

Although once thought to solely play a role in glycolysis, GAPDH is now considered to be a classic example of a moonlighting protein (Jeffery, 1999). Mammalian GAPDH has been implicated in many cellular activities, including apoptosis, nuclear RNA transport, DNA replication, DNA repair, RNase activity, microtubule bundling and membrane fusion (Sirover, 1996, 1997, 1999). Consistent with its many functions, GAPDH is thought to play roles in many diseases, including Parkinson's disease (PD), Alzheimer's disease, Huntington's disease, dentatorubropallidoluysian atrophy and prostate cancer (Sirover, 1996, 1997, 1999; Tatton, Chalmers-Redman, Brown *et al.*, 2003; Tatton, Chalmers-Redman & Tatton, 2003; Carlile *et al.*, 2000; Kragten *et al.*, 1998; Burke *et al.*, 1996).

The involvement of GAPDH in apoptosis is particularly intriguing because apoptosis is one mechanism of neuronal cell death that is thought to contribute to neurodegenerative diseases such as PD (Hara *et al.*, 2005; Tatton, Chalmers-Redman, Brown *et al.*, 2003; Tatton, Chalmers-Redman & Tatton, 2003; Carlile *et al.*, 2000; Kragten *et al.*, 1998; Saunders *et al.*, 1999; Berry & Boulton, 2000; Ishitani *et al.*, 2003; Maruyama *et al.*, 2001; Dastoor & Dreyer, 2001). The recent discovery of the NO–*S*-nitrosylation–GAPDH–Siah1 cascade answers two major outstanding questions about the role of GAPDH in apoptosis (Hara *et al.*, 2005). Firstly, nuclear accumulation of GAPDH had long been observed in cells stimulated to undergo apoptosis; however, the mechanism of nuclear translocation was unknown since GAPDH lacks a nuclear localization signal. Hara and coworkers showed that GAPDH enters the nucleus following *S*-nitrosylation of the active-site Cys by nitric oxide (NO) and binding to the E3 ubiquitin ligase Siah1, which does contain a nuclear localization signal (Hara *et al.*, 2005). Thus, GAPDH gains entry into the nucleus by virtue of Siah1's nuclear localization signal. The second major question about GAPDH and apoptosis concerns the role of nuclear GAPDH in apoptosis. The work of Hara and coworkers suggests that GAPDH stabilizes the otherwise short-lived Siah1, which leads to increased degradation of nuclear targets and promotion of apoptosis.

Small-molecule compounds that interfere with the pro-apoptotic activity of GAPDH by disrupting the NO–*S*-nitrosylation–GAPDH–Siah1 cascade are potential drug candidates for the treatment of PD and other neurodegenerative diseases. For example, the small-molecule compound CGP-3466 [dibenzo-(*b*,*f*)oxepin-10-ylmethyl-methyl-prop-2-ynyl-amine] reduces apoptosis by preventing nuclear localization of GAPDH (Tatton, Chalmers-Redman & Tatton, 2003; Katsube *et al.*, 1999; Kragten *et al.*, 1998); however, the molecular-level mechanism of CGP-3466 is poorly understood.

Knowledge of the three-dimensional structure of human GAPDH at high resolution would facilitate the development of specific inhibitors of GAPDHs from parasites as well as new anti-apoptosis drugs for the treatment of neurodegenerative diseases. Crystals of human liver GAPDH have been reported by one group (Warizaya *et al.*, 2004) and a moderate-resolution (2.5 Å) structure of the human liver enzyme has been determined by another (PDB code 1znq; Ismail & Park, 2005). Here, we report the 1.75 Å resolution structure of recombinant human placental GAPDH (HsGAPDH). The structure provides an updated view of the NAD^+-binding site, which is the target of inhibitors designed to combat parasitic diseases. The structure also provides a foundation for investigating the interactions between CGP-3466 and human GAPDH. Computational docking studies performed with our structure suggest plausible binding sites for CGP-3466 in the adenosine pocket of the NAD^+-binding site and a hydrophobic channel located at the intersection of the molecular twofold axes. We propose that binding of CGP-3466 in these sites may cause subtle tertiary and quaternary structural changes in GAPDH that decrease affinity for the E3 ubiquitin ligase Siah1, which would result in inhibition of the NO–GAPDH–Siah1 apoptosis cascade (Hara *et al.*, 2005). Finally, a qualitative model for the complex between GAPDH and Siah1 is proposed.

2. Materials and methods

2.1. Cloning, expression and purification

The pChug 20.2 construct (Vollberg *et al.*, 1989) was used to engineer a His-tagged HsGAPDH. PCR was used to amplify the HsGAPDH coding sequence of pChug 20.2 and to introduce *Nde*I and *Bam*HI restriction sites. The resulting fragment was subcloned into a pET14b vector (Novagen) that codes for an N-terminal hexahistidine tag (His_6). This His_6-HsGAPDH construct was introduced into the *Escherichia coli* expression strain BL21(DE3) pLysS. Protein was expressed by induction with isopropyl β-D-thiogalactopyranoside (IPTG) when the culture, which had been grown in LB broth containing carbenicillin and chloramphenicol, reached an optical density of approximately $A_{600} = 0.8$. Induction with IPTG lasted for 4 h at 310 K.

Pelleted *E. coli* cells were frozen overnight and resuspended the next day in lysis buffer (50 m*M* sodium phosphate pH 8.0 containing 10 m*M* imidazole, 1 m*M* phenylmethanesulfonyl fluoride and 0.3 *M* NaCl). The resuspended cells were disrupted by sonication in an ice-chilled container and benzonase nuclease (Novagen) was added to degrade nucleic acids released during sonication. The resulting cellular debris was removed by centrifugation at 10 000 rev min^{-1} for 25 min at 277 K followed by vacuum filtration through a 0.45 µm filter. Approximately 28 ml Ni–NTA resin (Qiagen) was added to the cleared supernatant and the mixture was stirred at 277 K for 4 h. The suspension was allowed to settle, the supernatant was decanted and the remaining slurry was poured into a gravity-flow column. Four column volumes of

wash buffer (50 m*M* sodium phosphate pH 8.0, 20 m*M* imidazole, 0.3 *M* NaCl) were applied to the packed column and the protein was eluted with 50 m*M* sodium phosphate pH 8.0, 250 m*M* imidazole, 0.3 *M* NaCl.

All fractions containing protein were analyzed by denaturing SDS–PAGE gels and those fractions containing His_6-HsGAPDH were combined and dialyzed overnight into 20 m*M* Tris pH 8.0. The protein was loaded onto a HiTrap Blue column (Amersham Pharmacia) that had been equilibrated with 20 m*M* Tris pH 8.0. The column was washed with the start buffer and HsGAPDH was eluted with the addition of 0.5 *M* NaCl in 20 m*M* Tris pH 8.0. The eluted fractions were pooled and dialyzed into the precrystallization buffer (2.5 m*M* Tris pH 7.7, 0.1 *M* NaCl, 1 m*M* β-mercaptoethanol, 1 m*M* disodium EDTA) supplemented with 10 m*M* NAD^+. To remove the His tag from the purified His_6-HsGAPDH, the protein was incubated with biotinylated thrombin (Novagen) for 12 h at 310 K. Streptavidin agarose and spin filters (Novagen) were used to remove the thrombin. The protein was batch purified as before with Ni–NTA and the fractions from the packing and wash steps containing the desired HsGAPDH were pooled. HsGAPDH was dialyzed into the precrystallization buffer and concentrated to 19.5 mg ml^{-1} using centrifugal filters and tubes (Millipore). Protein concentration was measured using the Bradford assay (Pierce).

Table 1
Data-collection and refinement statistics.

Values for the outer resolution shell are given in parentheses.

PDB code	1u8f
Wavelength (Å)	0.97857
Space group	$P2_12_12_1$
Unit-cell parameters (Å)	a = 84.95, b = 125.65, c = 132.33
Diffraction resolution (Å)	100–1.75 (1.81–1.75)
No. of observations	934983
No. of unique reflections	141888
Redundancy	6.6 (6.1)
Completeness (%)	99.6 (99.6)
Average $I/\sigma(I)$	23.0 (4.1)
$R_{merge}(I)$	0.071 (0.436)
No. of protein atoms	10 133
No. of NAD^+ molecules	3
No. of water molecules	911
R_{cryst}	0.191 (0.222)
R_{free}†	0.217 (0.259)
R.m.s.d.‡	
Bond lengths (Å)	0.0047
Bond angles (°)	1.39
Dihedral angles (°)	24.3
Improper dihedrals (°)	0.72
Ramachandran plot§	
Favored (%)	89.7
Allowed (%)	9.7
Generous (%)	0.3
Disallowed (%)	0.3
Average B factors (Å^2)	
Protein	15
NAD^+	22
Water	23

† 10% R_{free} test set. ‡ Compared with the Engh and Huber force field (Engh & Huber, 1991). § The Ramachandran plot was generated with *PROCHECK* (Laskowski *et al.*, 1993).

2.2. Crystallization and X-ray diffraction data collection

All crystallization experiments were performed at 295 K using the sitting-drop method of vapor diffusion. Initial crystallization conditions were obtained with Wizard, Hampton and Index screening kits. Several crystal forms were obtained for His_6-HsGAPDH. The most promising condition was 50% PEG 4000, 0.1 *M* HEPES buffer, 10% 2-propanol. Large crystals diffracted to only 3.4 Å resolution; therefore, the His_6 tag was cleaved and the untagged protein was used in crystal screening.

Screening of the untagged protein was very successful. For example, crystals appeared in approximately 36 of the 96 conditions of the Index Screen. Many of the screen conditions that produced crystals with His_6-HsGAPDH also gave crystals with untagged HsGAPDH. The crystals used for structure determination grew directly from Index Screen condition No. 89 (0.1 *M* succinic acid pH 7.0, 15% PEG 3350) in 4 d. These crystals were cryoprotected by the addition of reservoir solution supplemented with 15% glycerol. The cryoprotected crystals were frozen in liquid nitrogen.

Diffraction to 2.1 Å resolution was observed from frozen crystals using an in-house Cu rotating-anode diffraction system. The space group is $P2_12_12_1$, with unit-cell parameters a = 85, b = 126, c = 132 Å. There is one tetramer in the asymmetric unit and the solvent content is 45% (Matthews, 1968).

We note that attempts to crystallize His_6-HsGAPDH using the succinic acid/PEG 3350 recipe failed. Thus, removal of the affinity tag was critically important for obtaining high-quality crystals.

A 2.15 Å resolution data set was collected using an in-house Cu rotating-anode system. The data collection consisted of 235 frames with a crystal-to-detector distance of 175 mm, an oscillation angle of 0.5° and an exposure time of 10 min per frame. The *HKL* suite of programs (Otwinowski & Minor, 1997) was used to process the data. The final data set consisted of 309 453 observations of 77 527 unique reflections and was 99% complete to 2.15 Å resolution. The overall R_{merge} on I was 6.3%, with an average $I/\sigma(I)$ of 20.

Subsequently, a 1.75 Å resolution data set was collected at Advanced Photon Source (APS) beamline 19-ID. The data were processed with *HKL*2000 (Otwinowski & Minor, 1997). The data collection consisted of 930 frames obtained with a crystal-to-detector distance of 150 mm, an oscillation angle of 0.2° and an exposure time of 5 s per frame. The data set had excellent redundancy (6.6), completeness (99.6%) and signal-to-noise ratio [$I/\sigma(I)$ = 4 in the high-resolution bin]. Processing statistics for the APS data set are listed in Table 1.

2.3. Structure determination and refinement

Molecular replacement and initial model-building and refinement studies were performed with the 2.15 Å data set. Molecular-replacement calculations (10–4 Å) were performed with *AMoRe* (Navaza, 2001) using the *Thermus aquaticus*

GAPDH tetramer as the search model (PDB code 1cer; Tanner *et al.*, 1996). The *T. aquaticus* and HsGAPDH proteins share approximately 44% sequence identity. Calculations were carried out for all possible primitive orthorhombic space groups. Space group $P2_12_12_1$ gave the best molecular-replacement solution, as indicated by a correlation coefficient of 0.43 and *R* factor of 0.50. Rigid-body refinement in *CNS* (Brünger *et al.*, 1998) lowered the *R* factor to 0.48.

Phases from rigid-body refinement were input into *ARP/wARP* (Morris *et al.*, 2002) for automated model building using the 2.15 Å data set. Side chains were docked to the *ARP/wARP* model using the *guiSIDE* module of *CCP*4*i* (Potterton *et al.*, 2003). One complete subunit of the tetramer was built using *O* (Jones *et al.*, 1991) and non-crystallographic symmetry (NCS) was used to generate the full tetramer. The NCS of the tetramer can be described by three transformations that relate the *O* subunit to the *P*, *Q* and *R* subunits. The *O* subunit is related to the *P* subunit by a rotation in spherical polar coordinates of ($\psi = 80.3$, $\varphi = 72.0$, $\kappa = 178.9^\circ$) applied to the *O* chain followed by a translation of ($x = 71.7$, $y = 76.8$, $z = 37.1$ Å). The *O* and *Q* subunits are related by a rotation of ($\psi = 170.1$, $\varphi = 67.0$, $\kappa = 179.8^\circ$) and a translation of ($x = 69.6$, $y = -3.1$, $z = 48.8$ Å). The *O* and *R* subunits are related by a rotation of ($\psi = 90.3$, $\varphi = 162.0$, $\kappa = 179.9^\circ$) and a translation of ($x = -12.1$, $y = 71.5$, $z = 38.8$ Å). The model was completed in several rounds of model building using *O* followed by refinement against the APS 1.75 Å resolution data using *CNS* (Brünger *et al.*, 1998). Non-crystallographic symmetry restraints were not used during refinement. See Table 1 for refinement statistics.

The programs *CNS*, *O*, *CCP*4*i* and *PyMOL* (DeLano, 2002) were used for structural analysis. Superimposition of structures and root-mean-square difference (r.m.s.d.) calculations were performed using *CNS* and the websites for *CE* (Shindyalov & Bourne, 1998), *Mass* (Dror *et al.*, 2003) and *COMPARER* (Sali & Blundell, 1990).

2.4. CGP-3466 docking calculations

AutoDock v.3.0.5 (Goodsell *et al.*, 1996; Morris *et al.*, 1996) was used to identify plausible binding sites for CGP-3466 [dibenzo-(*b*,*f*)oxepin-10-ylmethyl-methyl-prop-2-ynyl-amine]. In preparation for these studies, solvent and NAD^+ were removed from the final refined HsGAPDH model and polar H atoms were added with *AutoDockTools* (*ADT*). A model of CGP-3466 (H atoms included) was built using the *PRODRG* server (van Aalten *et al.*, 1996). Partial charges for each atom of the protein and ligand were calculated with *ADT*. A global search for potential binding sites was performed using a $230 \times 230 \times 230$ point grid (0.375 Å grid spacing) that covered the entire HsGAPDH tetramer. Promising sites identified by the global docking search were explored further using smaller grids ($36 \times 36 \times 36$) focused on the sites of interest. Default parameters for the genetic algorithm–local search method of *AutoDock* were used for both the global and focused calculations with the following exceptions: translation step = 0.2 Å, quaternion step = 4.0°, torsion step = 4.0°, maximum number of energy evaluations = 1×10^7, number of generations = 2.7×10^4, number of survivors = 5.0 and number of runs = 100. The results were analyzed using the default cluster analysis in *ADT*. The *LPC* server was used to analyze interactions formed by the docked ligands and to calculate the surface area buried in ligand–protein interfaces (Sobolev *et al.*, 1999). The top CGP-3466 poses from focused docking runs have been deposited in the PDB (code 2feh).

2.5. GAPDH–Siah1 docking calculations

The web server for *PatchDock* was used to build qualitative models for the complex between HsGAPDH and the E3 ubiquitin ligase Siah1 in order to predict which protein surfaces might interact. The receptor for docking calculations was the HsGAPDH *QR* dimer, corresponding to two subunits related by the *P* molecular twofold axis. The ligand was the homodimer of murine Siah1a obtained from PDB entry 1k2f (Polekhina *et al.*, 2002). We note that 1k2f contains Siah1a residues 93–282, which includes the region that is essential for GAPDH–Siah1 complex formation (Hara *et al.*, 2005). Site-directed mutagenesis results from Hara and coworkers show that GAPDH residue Lys227 is essential for GAPDH–Siah1 association (Hara *et al.*, 2005); therefore, the docking calculations were constrained to return only complexes having Lys227 in the binding site. The top solution from *PatchDock* had a score of 10 388, which was 16% higher than the score for solution 2 (8992). For reference, solutions 3–5 had scores of 8854, 8206 and 8156.

3. Results

3.1. Quality of the model and overall fold

The structure reported here is one of the highest resolution GAPDH structures to date, exceeded only by the 1.7 Å structure of *Alcaligenes xylosoxidans* GAPDH (PDB code 1obf; Antonyuk *et al.*, 2003). Our structure is the highest resolution structure of a mammalian GAPDH. For comparison, structures of GAPDH from human liver (PDB code 1znq) and rabbit muscle (PDB code 1j0x; Cowan-Jacob *et al.*, 2003) have been determined at 2.5 and 2.4 Å, respectively.

The refined model consists of one tetramer with subunits labeled *O*, *P*, *Q* and *R*, containing 10 133 atoms, 1332 amino-acid residues, 911 water molecules and three NAD^+ molecules (Table 1). Dual side-chain conformations have been modeled for Glu93 (*O*, *P*, *Q*), Met*Q*103 and Cys*O*152. Disorder was found only in the two N-terminal residues and in the side chains of Lys*O*219 and Lys*Q*84.

The refinement statistics are consistent with a well refined and accurate crystal structure. For example, the *R* factor is 0.19 with $R_{\rm free} = 0.22$ for all reflections to 1.75 Å. The average protein *B* factors for individual subunits are 17.1 (*O*), 15.0 (*P*), 14.3 (*Q*) and 15.3 Å^2 (*R*). The root-mean-square deviations of bonds (0.0047 Å) and angles (1.4°) indicated excellent geometry and the stereochemistry meets or exceeds all the main-chain and side-chain tests of the *PROCHECK* package (Laskowski *et al.*, 1993). Only Ala150 (*O*, *P*, *R*) and Val240 (all four subunits) occupy the generously allowed or disallowed

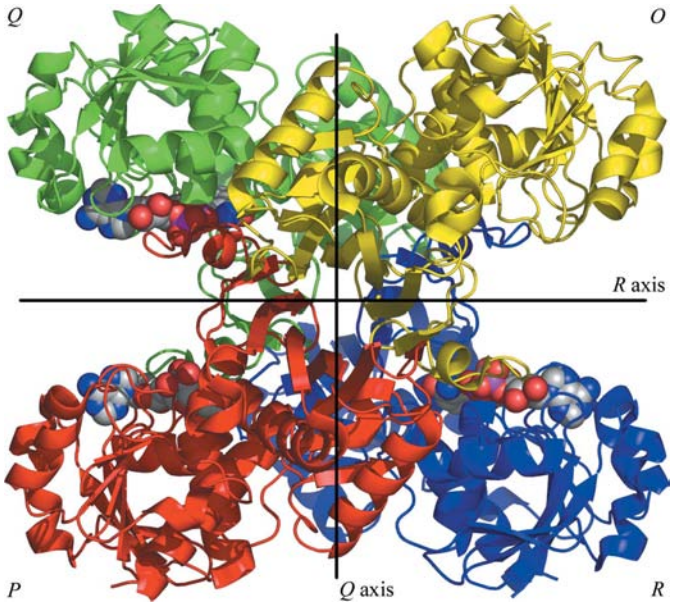

Figure 1
Ribbon drawing of the HsGAPDH tetramer viewed down the *P* axis. Lines indicate locations of the *Q* and *R* molecular twofold axes. The NAD^+ cofactors are drawn in CPK format.

regions of the Ramachandran plot. These residues appear in loops and they adopt similar conformations in other GAPDH structures (Shen *et al.*, 2000; Yun *et al.*, 2000; Kim *et al.*, 1995; Aronov *et al.*, 1999; Didierjean *et al.*, 1997; Skarzynski & Wonacot, 1988; Cowan-Jacob *et al.*, 2003).

The secondary, tertiary and quaternary structures of HsGAPDH are very similar to those of other GAPDH structures, as expected (Fig. 1). The tetramer displays approximate 222 symmetry, with each subunit consisting of an NAD^+-binding domain (residues 1–151, 315–335) and a catalytic domain (residues 152–314). The NAD^+-binding domain features the well known Rossmann dinucleotide-binding fold (Rossmann *et al.*, 1974), in which NAD^+ binds in an extended conformation (Fig. 2*a*) at the C-terminal edge of a parallel β-sheet that is flanked by helices on either side. The catalytic domain consists of a mixed twisted β-sheet flanked by three helices on one side. The other side of the β-sheet forms extensive intersubunit contacts with the β-sheet of the catalytic domain of an adjacent subunit. This so-called '*P* interface' is the largest of the three intersubunit interfaces of the tetramer and buries 7814 $Å^2$ of surface area in our structure. The *Q* and *R* interfaces bury 1824 and 5652 $Å^2$ of surface area, respectively.

The individual subunits of HsGAPDH are very similar to each other, as indicated by r.m.s.d. values of 0.50–0.66 Å for C^α atoms. The catalytic domains superimpose with r.m.s.d. values of 0.35–0.55 Å; the corresponding values for the NAD^+-binding domains are 0.55–0.67 Å.

The closest structural homologue to our enzyme is human liver GAPDH (PDB code 1znq, 100% amino-acid sequence identity to HsGAPDH) based on a search of the PDB using *SSM* (Krissinel & Henrick, 2004). The r.m.s.d.s between the subunits of our structure and those of 1znq are in the range 0.26–0.34 Å. The next closest homologue identified by *SSM* was another mammalian GAPDH, rabbit GAPDH (PDB code 1j0x; 95% amino-acid sequence identity to HsGAPDH). Subunits of 1j0x superimpose onto HsGAPDH with r.m.s.d. values of 0.28–0.68 Å. For reference, the r.m.s.d. values between HsGAPDH subunits and those of *T. aquaticus* GAPDH, which was used for molecular-replacement calculations, are 0.90–1.1 Å.

3.2. Active site

The active site of each subunit is located in a large cleft between the NAD^+-binding and catalytic domains. The Cys nucleophile (Cys152) resides at the N-terminus of the first helix of the catalytic domain. Electron-density maps clearly indicated the presence of NAD^+ bound with high occupancy in subunits *P*, *Q* and R (Fig. 2*a*). The average *B* factors for NAD^+ were 17 (*P*), 22 (*Q*) and 27 $Å^2$ (*R*). On the other hand, electron density for the cofactor in the *O* chain was very weak. Density representing the pyrophosphate was observed, but density features corresponding to the nicotinamide and adenosine groups were almost completely absent. Thus, NAD^+ was not modeled in the *O* subunit. Differential cofactor binding to GAPDH subunits has been observed previously and is presumably a consequence of the cooperativity of the enzyme (Duee *et al.*, 1996; Roitel *et al.*, 2003; Talfournier *et al.*, 1999). For example, three NAD^+ molecules are bound to the tetramer of *T. cruzi* GAPDH (PDB code 1ml3; Castilho *et al.*, 2003) and only two cofactor molecules are bound to the rabbit muscle GAPDH tetramer (PDB code 1j0x; Cowan-Jacob *et al.*, 2003).

Dual side-chain conformations were observed for Cys*O*152, which is presumably a consequence of the absence of NAD^+ in the *O* subunit. One conformation matches that found in the other subunits ($\chi_1 = 52^\circ$, occupancy = 0.7) and the other conformation corresponds to a relative rotation of 105° to $\chi_1 = -53^\circ$ (occupancy = 0.3). Note that the $\chi_1 = -53^\circ$ conformation for the nucleophilic Cys was also observed in the structure of *Palinurus versicolor* GAPDH (PDB code 1ihx; Shen *et al.*, 2002), which contains a bound NAD^+ analogue with disordered thionicotinamide ring. The authors suggested that movement of the catalytic Cys disrupted the highly conserved salt-bridge triad Arg13–Asp50–Glu317 (HsGAPDH numbering). We note that the triad is formed in all four subunits of our structure.

The NAD^+-binding sites of GAPDHs from pathogenic trypanosomatids are drug-design targets (Aronov *et al.*, 1998, 1999; Van Calenbergh *et al.*, 1995; Verlinde *et al.*, 1994; Bressi *et al.*, 2001; Suresh *et al.*, 2001). Knowledge of protein–NAD^+ interactions in human GAPDH is useful as a guide for developing highly specific anti-trypanosomatid drugs that do not inhibit human GAPDH. A schematic diagram of the interactions formed by NAD^+ in our structure is shown in Fig. 2(*b*). NAD^+ forms several noncovalent interactions that are also observed in other GAPDH structures. For example, the nicotinamide carbonyl forms a hydrogen bond with Asn316, while the nicotinamide amine forms an intramole-

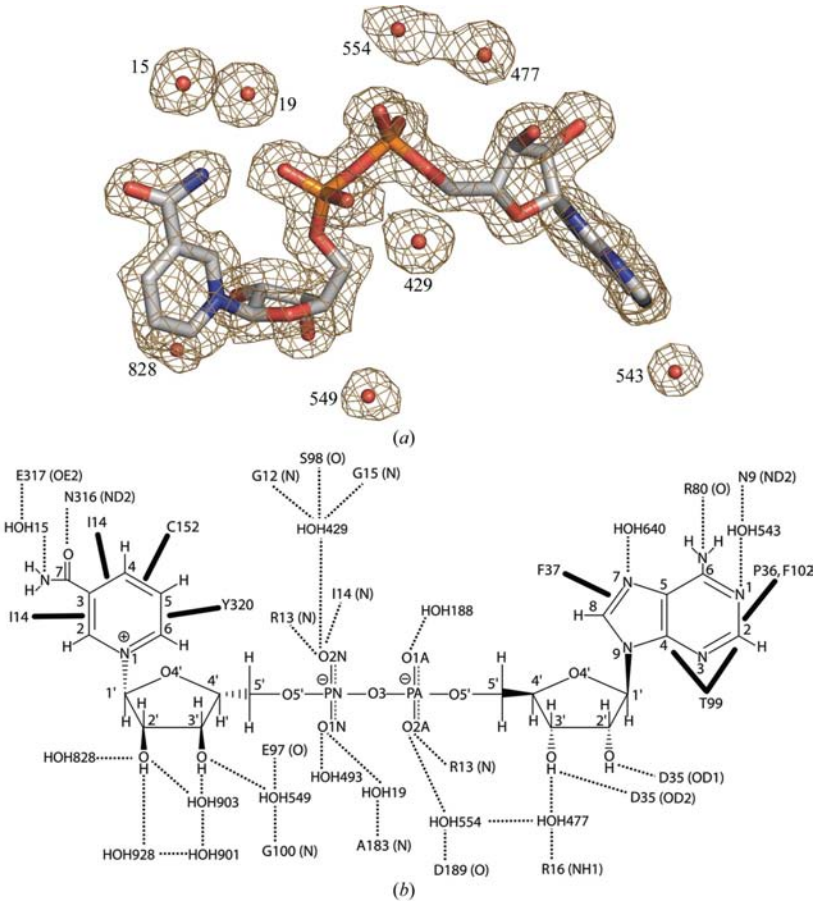

Figure 2
NAD^+ conformation and interactions. (*a*) NAD^+ and selected surrounding water molecules from the *P* subunit. The map is a simulated annealing σ_A-weighted $mF_o - DF_c$ electron-density map contoured at 3σ. The simulated-annealing calculation was started from the final model with NAD^+ and surrounding residues/water within 3.9 Å of NAD^+ omitted. (*b*) Schematic diagram of cofactor–protein interactions in the *P* subunit. The dotted lines indicate electrostatic interactions within 3.2 Å. The thick solid lines denote nonpolar contacts within 3.9 Å.

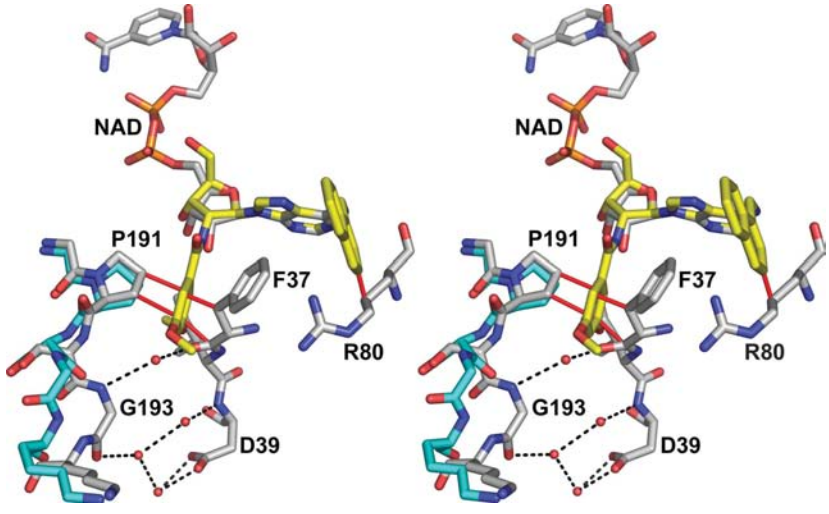

Figure 3
Model of the inhibitor NMDBA in the HsGAPDH active site (stereoview). The 1.75 Å HsGAPDH structure is shown in white. NMDBA is shown in yellow. Residues 191–193 of the 2.5 Å human liver GAPDH structure are shown in cyan. The dashed lines indicate the intersubunit water-mediated hydrogen bonds observed in HsGAPDH. The solid red lines indicate the predicted steric interference between the inhibitor and HsGAPDH (contact distance = 2.7 Å).

cular hydrogen bond with the pyrophosphate. As expected, the pyrophosphate binds in the glycine-rich loop of the Rossmann fold, which allows the pyrophosphate to form hydrogen bonds to the backbone amino groups of the N-terminal residues of the first helix of the Rossmann fold (Arg13, Ile14). The adenosine ribose forms two hydrogen bonds with the highly conserved Asp35. Nonpolar interactions with the cofactor aromatic rings are also observed. The nicotinamide ring contacts Ile14 and Tyr320, while the adenine contacts Pro36, Phe37, Thr99 and Phe102.

The exceptional quality of our electron-density maps allowed detailed modeling of solvent (Fig. 2*a*). For example, over a dozen water molecules interact with the cofactor (3.2 Å cutoff). Most of these water molecules mediate hydrogen bonds between NAD^+ and the protein (Fig. 2*b*). In contrast, the 2.5 Å human liver GAPDH structure has only three water molecules bound to NAD^+, which are equivalent to HOH15, HOH19 and HOH429 of our structure.

The highly conserved water molecule of the Rossmann fold (Bottoms *et al.*, 2002) is present in all four subunits of our structure (HOH425, HOH429, HOH227, HOH211). This water molecule is important because it bridges the pyrophosphate and the glycine-rich loop. The average *B* factor of the conserved water molecule is 17 $Å^2$, which is significantly lower than the average solvent *B* factor of 23 $Å^2$. Note that the conserved water molecule is present in the *O* chain, which does not contain a bound NAD^+. This result emphasizes that the conserved water molecule is an inherent structural feature of the Rossmann fold itself, as discussed previously (Bottoms *et al.*, 2002, 2005).

3.3. Selectivity cleft

One strategy for designing potent and selective inhibitors of trypanosomatid GAPDHs is to elaborate an adenosine framework with functional groups that bind in a narrow intersubunit 'selectivity cleft' that has been observed in the NAD^+-binding sites of GAPDHs from *T. brucei*, *T. cruzi* and *L. mexicana* (Aronov *et al.*, 1998, 1999; Van Calen-

bergh *et al.*, 1995; Verlinde *et al.*, 1994; Bressi *et al.*, 2001; Suresh *et al.*, 2001). It has been proposed that the selectivity cleft is closed in human GAPDH and thus inhibitors that fill the cleft of trypanosomatid GAPDHs could bind tightly to the desired target enzyme without inhibiting the human enzyme. This strategy has been realised, for example, in the disubstituted adenosine derivative NMDBA [N^6-(1-naphthalenemethyl)-2′-deoxy-2′-(3,5-dimethoxybenzamido)adenosine; Verlinde *et al.*, 1994; Suresh *et al.*, 2001; Aronov *et al.*, 1999].

In our structure, Phe37, Ile38 and Asp39 form one side of the cleft and Pro191, Ser192 and Gly193 from an adjacent subunit form the other side (Fig. 3). The cleft is only 4–5 Å wide in our structure, compared with 7–8 Å wide in the structure of *L. mexicana* GAPDH complexed with NMDBA. We superimposed NMDBA onto the adenine moiety of NAD^+ in our structure in order to examine the steric clashes that might prevent binding of the inhibitor to the human enzyme (Fig. 3). The O-2′ substituent of NMDBA is predicted to form steric clashes (contact distances = 1.1–2.7 Å) with cleft residues Phe37, Ile38 and Pro191 (Fig. 3). We also predict a steric clash of the inhibitor naphthalene group with Arg80. Although our modeling does not consider the possibility of induced-fit binding, the severity of the predicted clashes suggests that the selectivity cleft is effectively closed in HsGAPDH, which supports the strategy of leveraging this cleft in inhibitor design.

Interestingly, our structure shows a large conformational difference with the 2.5 Å human liver GAPDH structure (PDB code 1znq) in the cleft region. Residues 192–194 differ by 1.1–6.5 Å in the two structures, with the largest difference occurring at the carbonyl of Gly193 (Fig. 3). In fact, this section of the polypeptide chain represents the largest backbone difference between the two structures. This difference is possibly significant because Gly193 in our structure forms intersubunit interactions that help keep the cleft closed. For example, Gly193 links to the other side of the cleft *via* intersubunit water-mediated hydrogen bonds to the carbonyl of Phe37 and to the main chain and side chain of Asp39 (Fig. 3). These interactions cannot be formed in 1znq because the distance across the cleft at position 193 is too large.

3.4. Docking studies of CGP-3466

CGP-3466 is a deprenyl-related compound (Fig. 4) that inhibits the pro-apoptotic activity of GAPDH (Kragten *et al.*, 1998; Tatton, Chalmers-Redman & Tatton, 2003; Carlile *et al.*, 2000). However, the mechanism of inhibition and molecular-level details of the GAPDH–CGP-3466 interaction are not known. Therefore, we performed virtual docking calculations using our high-resolution HsGAPDH structure and a flexible model of CGP-3466 in order to generate hypotheses regarding plausible binding sites.

Using the entire GAPDH tetramer as the protein target, *AutoDock* identified 16 multi-member conformational clusters (MMCCs), which had docking scores in the range −46.0 to −33.9 kJ mol^{-1}. Two regions of the protein clearly stood out as potential CGP-3466-binding sites: the adenosine pocket (ADE) of the NAD^+-binding site and the central channel (CCH) located near the intersection of the three molecular twofold axes (Fig. 1). Five of the 16 MMCCs, corresponding to 24 of the 100 docking runs, were located in the adenosine pocket of an NAD^+-binding site. These docked poses had scores in the range −39.7 to −37.2 kJ mol^{-1}. Another five MMCCs, which represented 18 of the 100 docking runs, were located in the central channel. The central channel poses corresponded to the top ten docking scores (−46.0 to −40.1 kJ mol^{-1}). Thus, the adenosine pocket and central channel together accounted for almost two-thirds of the 16 MMCCs and nearly half of the 100 docking runs. No other region of the protein was implicated with a higher frequency or better docking score by our initial docking calculation.

To complement and validate the global docking results, we used *CASTP* (Binkowski *et al.*, 2003) to survey the surface topography of the tetramer in order to identify pockets large enough to serve as ligand-binding sites. CASTP found 157 pockets in the GAPDH tetramer. These pockets had surface areas in the range 1–3514 Å^2, with an average of 120 Å^2. The pocket volumes were in the range 3–7814 Å^3, with an average volume of 191 Å^3 (Fig. 5). Note that the two largest pockets each correspond to two NAD-binding sites, which explains their large *CASTP* volumes (>7500 Å^3). Only three of the pockets identified by *CASTP* are large enough to accommodate CGP-3466, which has a molecular volume of 255 Å^3: the NAD^+-binding site, the central channel and a surface indentation located near the 274–277 β-strand (Fig. 5).

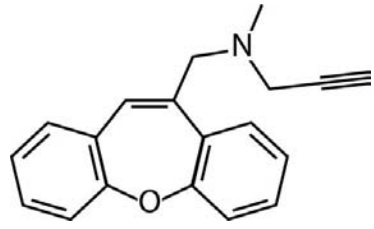

Figure 4
Chemical structure of CGP-3466.

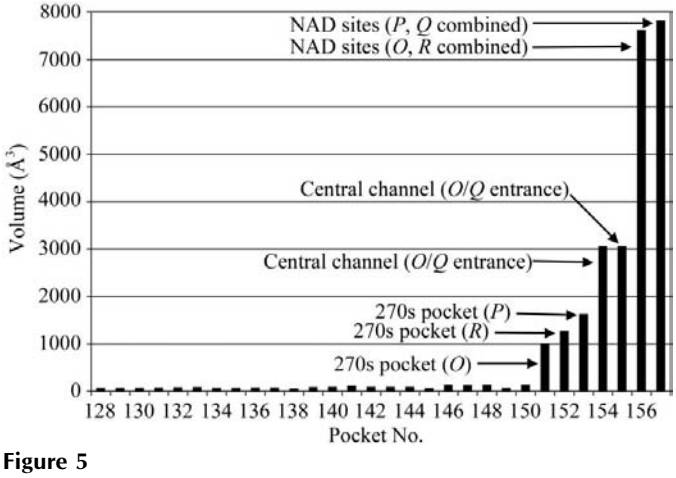

Figure 5
CASTP analysis of HsGAPDH pockets. The plot shows the volumes of the 30 largest pockets found by *CASTP*. Locations of pockets with significant volume are indicated.

Table 2
Summary of CGP-3466 docking results.

Ligand pose	Location	Docking score (kJ mol^{-1})	Cluster size†	Buried surface area‡ (%)	Contact residues
CCH46§	Central channel	−46.0	80	94	Leu203, Gln204, Pro236, Thr237, Ala238¶, Asn239, Ser283, Ser284, Asn287
CCH60	Central channel	−43.1	10	94	Ser51, Thr52, Leu203, Gln204¶, Pro236, Thr237, Ala238, Asn239, Asn287
ADE79§	Adenosine pocket	−39.3	38	82	Asn9, Gly10, Gly12, Asn34, Asp35, Pro36, Phe37, Pro191, Arg80, Thr99, Val101, Phe102
ADE69	Adenosine pocket	−38.5	25	76	Asn9, Gly10, Gly12, Asn34, Asp35, Pro36, Phe37, Arg80, Thr99, Val101, Phe102
ADE42	Adenosine pocket	−37.2	15	80	Asn9, Gly10, Gly12, Asn34, Asp35, Pro36, Phe37, Thr99, Val101, Phe102

† Refers to a 100-run docking calculation focused on the indicated location. ‡ Expressed as a percentage of the solvent-accessible surface area of the uncomplexed ligand. § Denotes lowest energy conformation of a 100-run docking calculation focused on the indicated location. ¶ Forms hydrogen bond with docked ligand.

The 270s pocket identified by *CASTP* is a shallow bowl-shaped indentation near a region of the protein that contains a novel CRM1-mediated nuclear-export signal (Brown *et al.*, 2004). The β-strand consisting of Leu274, Gly275, Tyr276 and Thr277 forms the bottom of the bowl. The rim of the bowl is formed by Lys263, Glu267, Lys271, Glu278, His279, Phe286, His291 and Thr294 of one subunit and Tyr49 and Lys55 from an NCS-related (*Q*-axis) subunit. In our global docking calculation, this site corresponded to two MMCCs, representing five out of 100 docking runs. The docking scores were in the range −36.4 to −34.7 kJ mol^{-1}. Although this site is large enough to accommodate CGP-3466, it is quite hydrophilic owing to the many charged and polar residues of the rim, which seems incompatible with binding a very hydrophobic molecule like CGP-3466.

Since the adenosine pocket and central channel were implicated by both the global docking calculation and *CASTP* and these sites are appropriately hydrophobic, they were explored further using focused docking calculations. The focused calculations each consisted of 100 docking runs and employed smaller grids centered on the regions of interest. Results of these calculations are summarized in Table 2 and Fig. 6.

A docking calculation focused on the adenosine pocket revealed three major clusters of poses, which had energies in the range −39.3 to −37.2 kJ mol^{-1} (Table 2). The docked ligands are 76–82% buried and the CGP-3466 ring system occupies the same location as the adenine ring system of NAD$^+$ (Fig. 6*a*). The overlap between adenine and the CGP-3466 ring system is particularly good for the two lowest energy conformations, ADE79 and ADE69 (Fig. 6*a*). Residues forming major contacts with all three clusters of docked ligands, based on hydrophobic ligand–protein contact-surface area calculated with *LPC* (Sobolev *et al.*, 1999), include Pro36, Phe37, Thr99, Val101 and Phe102. Note that residues 36, 37, 99 and 102 also form hydrophobic contacts with the NAD$^+$ adenine (Fig. 2*b*).

The docking calculation focused on the central channel produced the top docking scores of our study. This calculation revealed two major poses, which together accounted for 90 of the 100 docking runs (Table 2; CCH46 and CCH60). The docked ligands are almost completely buried (94%) and contact several residues (Table 2, Fig. 6*b*). The binding site exhibits symmetry owing to its location near the intersection of the molecular twofold axes and thus all four chains contribute to the site. The major contact residues for CCH46 are Leu203 (*P*, *R*), Gln204 (*P*, *R*), Thr237 (*O*, *Q*), Asn239 (*O*) and Ala238 (*O*) (Fig. 6*b*). Major contact residues for CCH60 are Leu203 (*P*, *R*), Gln204 (*P*, *R*), Ala238 (*O*, *Q*), Asn239 (*O*, *Q*) and Thr52 (*Q*) (Fig. 6*b*). In addition, the heteroatom O atoms of CCH46 and CCH60 are predicted to form hydrogen bonds with Ala238 and Gln204, respectively (Fig. 6*b*).

Note that three additional equivalent central channel binding sites are related by twofold rotations around the *P*, *Q* and *R* axes of the tetramer. In fact, the *CASTP* analysis revealed that the central channel actually consists of two distinct symmetry-related chambers having separate entrances located at opposite ends of the *Q* axis (Figs. 5). Division of the central channel into two chambers is caused by a constriction of the channel at the center of the tetramer.

3.5. Structural insights into GAPDH–Siah1 interaction

Truncation mutagenesis data suggest that GAPDH residues 222–240 and Siah1 residues 270–282 are essential for GAPDH–Siah1 association (Hara *et al.*, 2005). Moreover, mutagenesis of GAPDH Lys227 abrogates GAPDH–Siah1 complex formation (Hara *et al.*, 2005), which suggests that Lys227 directly interacts with Siah1 in the interface between the two proteins.

GAPDH residues 222–240 begin with a solvent-exposed loop (residues 222–227) and continue through a β-strand (228–234) that travels toward the central channel, finishing in a loop (residues 235–240) inside the channel (Fig. 7*a*). This β-strand is part of the mixed twisted β-sheet of the catalytic domain that forms the extensive *P* interface and thus it makes critical intersubunit interactions. Note that Lys227 is located on a solvent-exposed loop (Fig. 7*a*), which is consistent with its predicted involvement in complex formation. On the other hand, the β-strand (residues 228–234) and the central channel would be inaccessible to Siah1, assuming GAPDH retains the tetrameric form that we observe in the crystal structure.

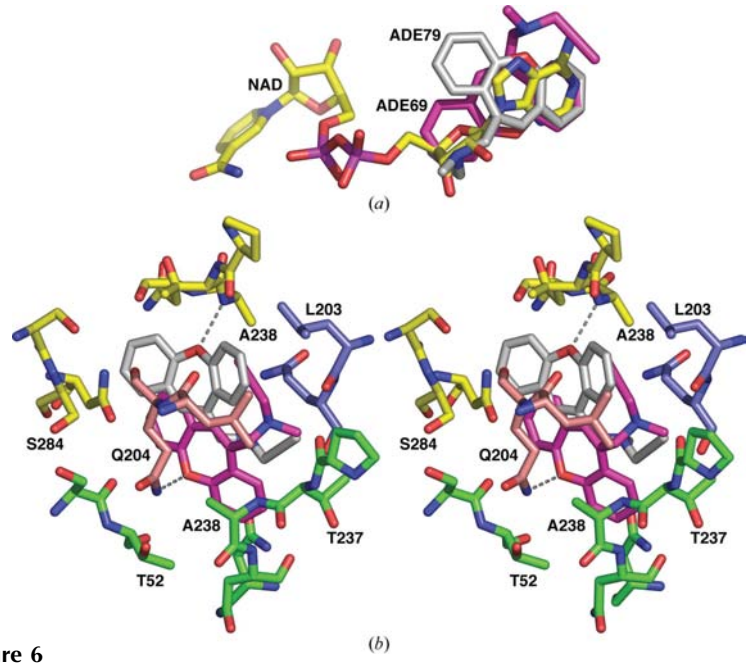

Figure 6
Predicted binding sites for CGP-3466. (*a*) Adenosine pocket. Docked CGP-3466 poses ADE79 and ADE69 are shown in white and magenta, respectively. For reference, NAD^+ is included in yellow. (*b*) Detailed stereoview of the predicted CGP-3466-binding site in the central channel. GAPDH subunits are colored as follows: *O*, yellow; *P*, pink; *Q*, green; *R*, blue. Docked CGP-3466 poses CCH46 and CCH60 are shown in white and magenta, respectively.

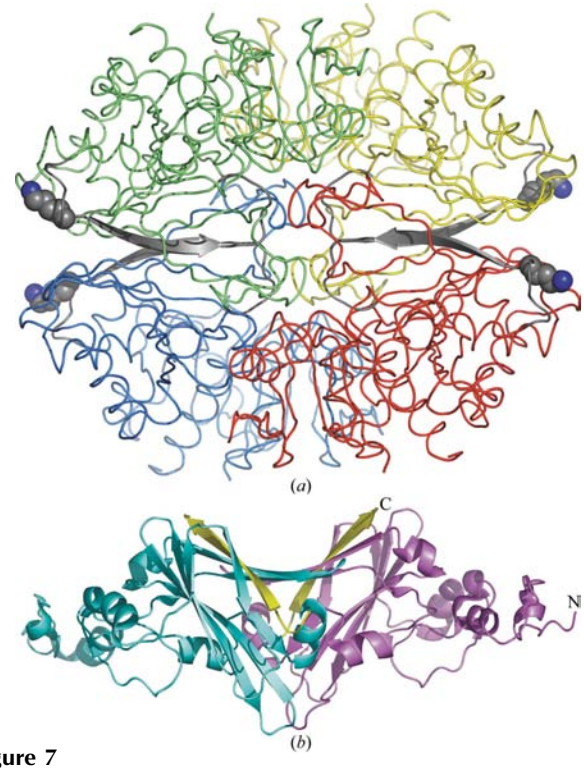

Figure 7
Structures of HsGAPDH and Siah1 highlighting regions that are important for GAPDH–Siah1 association. (*a*) HsGAPDH tetramer viewed down the *R* axis. Subunits are colored as follows: *O*, yellow; *P*, red; *Q*, green; *R*, blue. Residues that are essential for complex formation with Siah1 are colored gray (residues 222–240) and atoms of Lys227 are drawn as spheres. (*b*) Homodimer of Siah1 from PDB entry 1k2f (Polekhina *et al.*, 2002). The two subunits of Siah1 are colored cyan and violet. Residues that are essential for interaction with GAPDH are colored yellow (residues 270–282).

Siah1 residues 270–282 form the last β-strand (β8) of a curved antiparallel four-stranded β-sheet located in the C-terminus of the protein (see Fig. 7*b* and Polekhina *et al.*, 2002). This β-sheet joins with the analogous sheet from the opposite subunit of the Siah1 dimer to form an intermolecular β-sheet, which results in a large (30 Å wide) shallow groove (Fig. 7*b*).

We used the protein–protein docking program *PatchDock* to build a qualitative model of the GAPDH–Siah1 complex, subject to the constraint that GAPDH Lys277 is in the binding interface. Interestingly, the complex having the top score from *PatchDock* featured the large shallow groove of Siah1 contacting the convex surface of GAPDH near Lys227 (Fig. 8*a*). In this model, GAPDH Lys227 interacts with Siah1 β8 *via* a hydrogen bond with the hydroxyl of Siah1 Ser280 (Fig. 8*a*). Thus, our model is consistent with the experimental data of Hara and coworkers, which implicates GAPDH Lys227 and Siah1 β8 as being essential for GAPDH–Siah1 association. Moreover, the model is consistent with the assertion of Polekhina and coworkers that the large shallow groove of Siah1 plays a role in recognizing and interacting with other proteins (Polekhina *et al.*, 2002).

We expanded the GAPDH–Siah1 model using the symmetry of the GAPDH tetramer and found that no steric clashes were introduced (Figs. 8*b* and 8*c*). The expanded model contains one GAPDH tetramer interacting with four Siah1 dimers. Note that our model implies a binding stoichiometry of 1:2 (GAPDH:Siah1), which could be tested experimentally.

4. Discussion

Our main motivation for engineering a recombinant HsGAPDH and determining a high-resolution crystal structure was to provide a better structural foundation for drug-design and biophysical studies related to GAPDH's moonlighting functions. When we started this work, the only human GAPDH structure in the PDB was Watson's 3.5 Å structure of the human skeletal muscle enzyme determined from twinned crystals (Mercer *et al.*, 1976). Since then, a structure of human liver GAPDH has been deposited in the PDB (PDB code 1znq; Ismail & Park, 2005). However, the crystallographic resolution of 1znq is only 2.5 Å and the structure was determined from a data set with modest completeness (82% overall, 58% in the high-resolution bin). Thus, our structure is the highest resolution structure of a human (or mammalian) GAPDH to date and represents a significant improvement over previously available models.

4.1. Selectivity cleft

Our structure provides the first high-resolution view of a human GAPDH cofactor-binding site, which is relevant to design of inhibitors that specifically target trypanosomatid GAPDHs. In particular, we examined the proposed 'selectivity cleft' near the adenosine-binding site and found it to be 3–4 Å narrower than that of *L. mexicana* GAPDH; that is, effectively closed.

Moreover, our structure revealed a new feature of the cleft: water-mediated intersubunit hydrogen bonds. These interactions appear to help maintain the cleft in the closed conformation and thus represent a structural determinant of the selectivity of NMDBA and similar drugs towards trypanosomatid GAPDHs. These interactions are not present in the human liver GAPDH structure owing to large conformational differences at residues 192–195 (Fig. 3). We note that the conformation of residues 192–195 of rabbit GAPDH (PDB code 1j0x) is similar to that of our structure, although the intricate water-mediated hydrogen-bond network was not observed in 1j0x owing, perhaps, to its moderate crystallographic resolution of 2.4 Å.

The underlying reason for the large conformational difference between the two human GAPDH structures is unclear. Neither structure is compromised by crystal contacts in this particular region. It may be that the difference reflects an inherent flexibility in this region of the protein. It remains to be seen whether such flexibility might allow certain anti-trypanosomatid GAPDH inhibitors to bind to the human enzyme.

4.2. Docking studies of CGP-3466

CGP-3466 inhibits the pro-apoptotic activity of GAPDH by preventing nuclear localization of GAPDH. Since the molecular mechanism of this compound is poorly understood, we performed *in silico* docking studies in order to gain hypotheses about potential binding sites.

Our calculations predicted the adenosine pocket as a possible binding site, which is consistent with the observation that binding of rabbit GAPDH to immobilized CGP-3466 is inhibited by NAD^+ as measured by surface plasmon resonance (Kragten *et al.*, 1998). Also, Cowan-Jacob *et al.* (2003) reported crystallographic evidence for binding of CGP-3466 to the adenosine pocket of rabbit GAPDH; however, the electron density representing the inhibitor was extremely weak and consequently CGP-3466 was not included in PDB entry 1j0x. Interestingly, one of the ligand orientations identified by our study (ADE69) is very similar to that reported by Cowan-

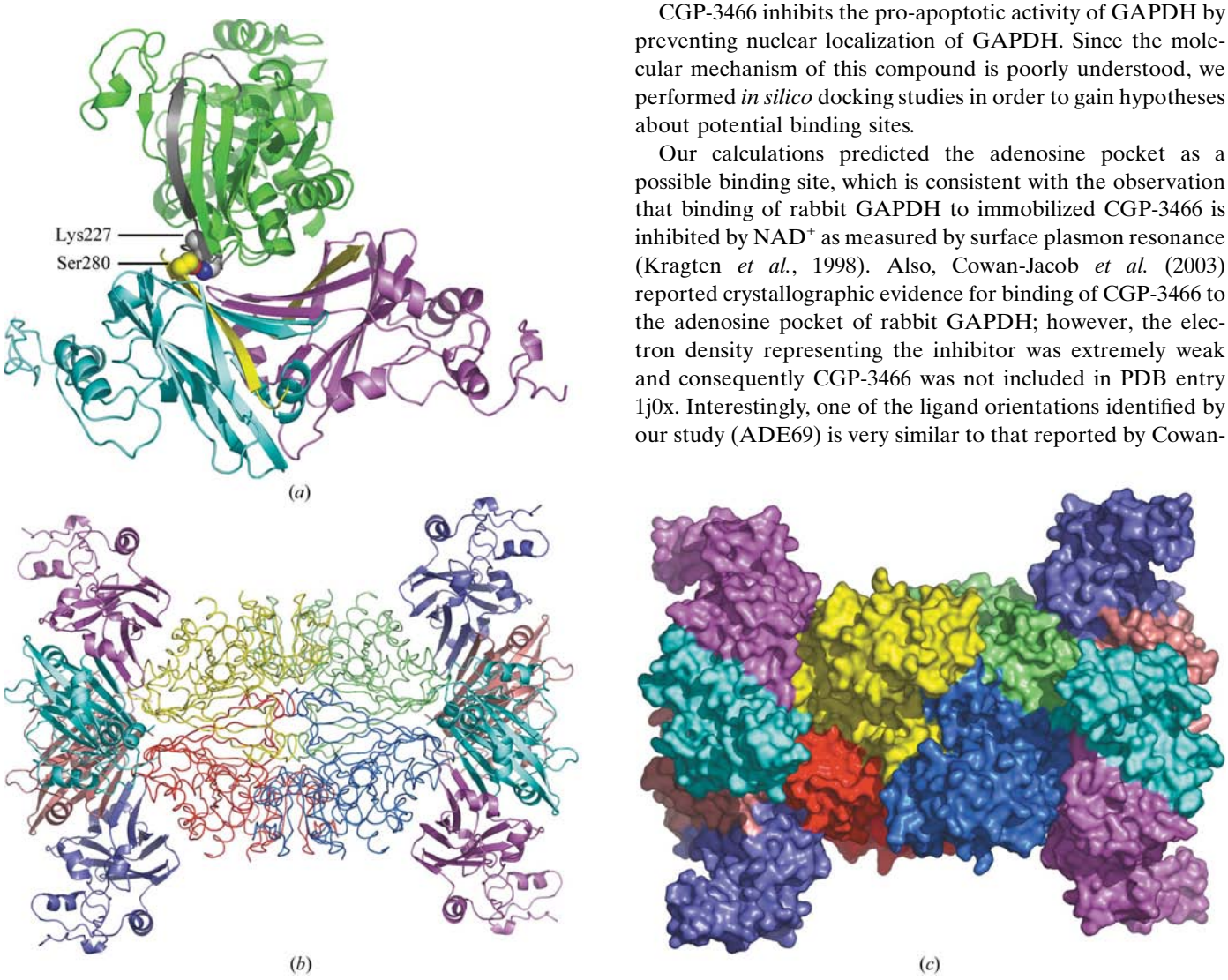

Figure 8
Qualitative model of the HsGAPDH–Siah1 complex. (*a*) Docked complex having the top score from *PatchDock*. A GAPDH subunit is shown in green and the Siah1 dimer is shown in cyan/violet. Only one subunit of the GAPDH dimer used for docking is shown for clarity. GAPDH residues 222–240 are colored gray. Siah1 residues 270–282 are colored yellow. GAPDH Lys227 and Siah1 Ser280 are drawn as spheres. (*b*) Model of a GAPDH tetramer interacting with four Siah1 dimers. This model was generated from the model in (*a*) using the symmetry of the GAPDH tetramer. The view is looking down the GAPDH *R* axis. GAPDH subunits are colored as follows: *O*, yellow; *P*, red; *Q*, green; *R*, blue. Siah1 dimers are colored cyan/violet and salmon/slate. (*c*) Surface representation of the model shown in (*b*).

Jacob *et al.* (2003), which provides additional support for the adenosine pocket as a potential binding site for CGP-3466. Site-directed mutagenesis of Pro36, Phe37, Thr99, Val101 and Phe102 could be used to test the importance of this proposed binding site.

Our docking calculations also suggested the central channel as a plausible binding site for CGP-3466. In fact, this site produced the best docking scores. This prediction is consistent with the experimental work of Carlile and coworkers, which showed that an antibody raised against residues that block the channel entrance prevent binding of BODIPY-labeled CGP-3466 (Carlile *et al.*, 2000). Primary candidates for site-directed mutagenesis studies to test the importance of this binding site include Leu203 and Gln204.

4.3. NO–*S*-nitrosylation–GAPDH–Siah1 cascade

Hara and coworkers showed that nitrosylation of the GAPDH active-site Cys (−SNO) enhances GAPDH–Siah1 association (Hara *et al.*, 2005). Hydrolysis of *S*-nitrosylated GAPDH produces various oxidized forms such as the sulfenic (−SOH), sulfinic ($-SO_2H$) and sulfonic ($-SO_3H$) acids. The latter form of GAPDH was isolated from apoptotic HEK293 cells and identified by mass spectrometry (Hara *et al.*, 2005). Presumably, modification of the active-site Cys causes conformational changes in GAPDH that enhance GAPDH–Siah1 interaction. However, it is unlikely that this rather small chemical modification produces large conformational changes in GAPDH. In fact, the sulfonic acid form of the active-site Cys is present in the crystal structure of *A. xylosoxidans* GAPDH (PDB code 1obf; Antonyuk *et al.*, 2003). This protein displays the classic GAPDH tetrameric form with no significant global structural changes (Antonyuk *et al.*, 2003). Thus, it is not clear why *S*-nitrosylation and subsequent oxidation of GAPDH promotes association with Siah1.

Discovery of the NO–GAPDH–Siah1 cascade forces rethinking of the mechanisms of anti-apoptosis compounds such as CGP-3466. Experimental work and molecular modeling, including our docking study, predict CGP-3466-binding sites in the adenosine pocket and central channel. There are at least two plausible mechanisms by which CGP-3466 binding in the cofactor site could disrupt the NO–GAPDH–Siah1 cascade. Firstly, CGP-3466 could protect the active-site Cys from reaction with NO. Secondly, binding of CGP-3466 in the cofactor site could cause a change in the tertiary and/or quaternary structure of GAPDH that reduces GAPDH–Siah1 affinity. This scenario is plausible because binding of NAD^+ is known to cause tertiary and quaternary structural changes that underlie cooperativity (Duee *et al.*, 1996; Leslie & Wonacott, 1984).

Considering the proposed central channel binding site for CGP-3466, the channel itself is too narrow for Siah1 to enter and thus it is unlikely that CGP-3466 competes with Siah1 for a central channel binding site. Given that the central channel is located within intersubunit interfaces, it seems more likely that binding of CGP-3466 in the central channel causes quaternary structural adjustments that decrease the GAPDH–Siah1 affinity. We note that our model of GAPDH–Siah1 shows Siah1 dimers packed closely together on the surface of GAPDH (Figs. 8*b* and 8*c*). Thus, subtle changes in GAPDH quaternary structure could cause steric interference between the bound Siah1 dimers. Ultimately, biophysical and structural studies will be needed to understand the details of GAPDH–Siah1 association and to design drugs that intersect the NO–GAPDH–Siah1 cascade.

Predoctoral support for JLJ was provided in part by the National Science Foundation and MAGEP (Missouri Alliance for Graduate Education and the Professorate). We thank M. A. Sirover for his generous gift of pChug 20.2 and Ming-Yi Zhou of the DNA Core Facility at the University of Missouri-Columbia for preparation of the HsGAPDH plasmid. We thank the personnel of APS beamline 19-ID for assistance with data collection, especially Stephen L. Ginell. Use of the Argonne National Laboratory Structural Biology Center beamlines at the APS was supported by the US Department of Energy, Office of Energy Research under Contract No. W-31-109-ENG-38.

References

Aalten, D. M. van, Bywater, R., Findlay, J. B., Hendlich, M., Hooft, R. W. & Vriend, G. (1996). *J. Comput.-Aided Mol. Des.* **10**, 255–262.
Antonyuk, S. V., Eady, R. R., Strange, R. W. & Hasnain, S. S. (2003). *Acta Cryst.* D**59**, 835–842.
Aronov, A. M., Suresh, S., Buckner, F. S., Van Voorhis, W. C., Verlinde, C. L., Opperdoes, F. R., Hol, W. G. & Gelb, M. H. (1999). *Proc. Natl Acad. Sci. USA*, **96**, 4273–4278.
Aronov, A. M., Verlinde, C. L., Hol, W. G. & Gelb, M. H. (1998). *J. Med. Chem.* **41**, 4790–4799.
Berry, M. D. & Boulton, A. A. (2000). *J. Neurosci. Res.* **60**, 150–154.
Binkowski, T. A., Naghibzadeh, S. & Liang, J. (2003). *Nucleic Acids Res.* **31**, 3352–3355.
Bottoms, C. A., Smith, P. E. & Tanner, J. J. (2002). *Protein Sci.* **11**, 2125–2137.
Bottoms, C. A., White, T. A. & Tanner, J. J. (2006). Submitted.
Bressi, J. C., Verlinde, C. L., Aronov, A. M., Shaw, M. L., Shin, S. S., Nguyen, L. N., Suresh, S., Buckner, F. S., Van Voorhis, W. C., Kuntz, I. D., Hol, W. G. & Gelb, M. H. (2001). *J. Med. Chem.* **44**, 2080–2093.
Brown, V. M., Krynetski, E. Y., Krynetskaia, N. F., Grieger, D., Mukatira, S. T., Murti, K. G., Slaughter, C. A., Park, H. W. & Evans, W. E. (2004). *J. Biol. Chem.* **279**, 5984–5992.
Brünger, A. T., Adams, P. D., Clore, G. M., DeLano, W. L., Gros, P., Grosse-Kunstleve, R. W., Jiang, J.-S., Kuszewski, J., Nilges, M., Pannu, N. S., Read, R. J., Rice, L. M., Simonson, T. & Warren, G. L. (1998). *Acta Cryst.* D**54**, 905–921.
Burke, J. R., Enghild, J. J., Martin, M. E., Jou, Y. S., Myers, R. M., Roses, A. D., Vance, J. M. & Strittmatter, W. J. (1996). *Nature Med.* **2**, 347–350.
Callens, M. & Hannaert, V. (1995). *Ann. Trop. Med. Parasitol.* **89**, 23–30.
Carlile, G. W., Chalmers-Redman, R. M., Tatton, N. A., Pong, A., Borden, K. E. & Tatton, W. G. (2000). *Mol. Pharmacol.* **57**, 2–12.
Castilho, M. S., Pavao, F., Oliva, G., Ladame, S., Willson, M. & Perie, J. (2003). *Biochemistry*, **42**, 7143–7151.
Cowan-Jacob, S. W., Kaufmann, M., Anselmo, A. N., Stark, W. & Grutter, M. G. (2003). *Acta Cryst.* D**59**, 2218–2227.
Dastoor, Z. & Dreyer, J. L. (2001). *J. Cell Sci.* **114**, 1643–1653.

Daubenberger, C. A., Poltl-Frank, F., Jiang, G., Lipp, J., Certa, U. & Pluschke, G. (2000). *Gene*, **246**, 255–264.
DeLano, W. L. (2002). *The PyMOL Molecular Graphics System.* http://www.pymol.org.
Didierjean, C., Rahuel-Clermont, S., Vitoux, B., Dideberg, O., Branlant, G. & Aubry, A. (1997). *J. Mol. Biol.* **268**, 739–759.
Dror, O., Benyamini, H., Nussinov, R. & Wolfson, H. (2003). *Bioinformatics*, **19**, *Suppl.* 1, i95–i104.
Duee, E., Olivier-Deyris, L., Fanchon, E., Corbier, C., Branlant, G. & Dideberg, O. (1996). *J. Mol. Biol.* **257**, 814–838.
Engh, R. A. & Huber, R. (1991). *Acta Cryst.* A**47**, 392–400.
Goodsell, D. S., Morris, G. M. & Olson, A. J. (1996). *J. Mol. Recognit.* **9**, 1–5.
Hara, M. R., Agrawal, N., Kim, S. F., Cascio, M. B., Fujimuro, M., Ozeki, Y., Takahashi, M., Cheah, J. H., Tankou, S. K., Hester, L. D., Ferris, C. D., Hayward, S. D., Snyder, S. H. & Sawa, A. (2005). *Nature Cell Biol.* **7**, 665–674.
Ishitani, R., Tajima, H., Takata, H., Tsuchiya, K., Kuwae, T., Yamada, M., Takahashi, H., Tatton, N. A. & Katsube, N. (2003). *Prog. Neuropsychopharmacol. Biol. Psychiatry*, **27**, 291–301.
Ismail, S. A. & Park, H. W. (2005). *Acta Cryst.* D**61**, 1508–1513.
Jeffery, C. J. (1999). *Trends Biol. Sci.* **24**, 8–11.
Jones, T. A., Zou, J.-Y., Cowan, S. W. & Kjeldgaard, M. (1991). *Acta Cryst.* A**47**, 110–119.
Katsube, N., Sunaga, K., Aishita, H., Chuang, D. M. & Ishitani, R. (1999). *J. Pharmacol. Exp. Ther.* **288**, 6–13.
Kim, H., Feil, I. K., Verlinde, C. L. M. J., Petra, P. H. & Hol, W. G. J. (1995). *Biochemistry*, **34**, 14975–14986.
Kim, H. & Hol, W. G. (1998). *J. Mol. Biol.* **278**, 5–11.
Kragten, E., Lalande, I., Zimmermann, K., Roggo, S., Schindler, P., Muller, D., van Oostrum, J., Waldmeier, P. & Furst, P. (1998). *J. Biol. Chem.* **273**, 5821–5828.
Krissinel, E. & Henrick, K. (2004). *Acta Cryst.* D**60**, 2256–2268.
Ladame, S., Castilho, M. S., Silva, C. H., Denier, C., Hannaert, V., Perie, J., Oliva, G. & Willson, M. (2003). *Eur. J. Biochem.* **270**, 4574–4586.
Laskowski, R. A., MacArthur, M. W., Moss, D. S. & Thornton, J. M. (1993). *J. Appl. Cryst.* **26**, 283–291.
Leitao, A., Andricopulo, A. D., Oliva, G., Pupo, M. T., de Marchi, A. A., Vieira, P. C., da Silva, M. F., Ferreira, V. F., de Souza, M. C., Sa, M. M., Moraes, V. R. & Montanari, C. A. (2004). *Bioorg. Med. Chem. Lett.* **14**, 2199–2204.
Leslie, A. G. W. & Wonacott, A. J. (1984). *J. Mol. Biol.* **178**, 743–772.
Marchi, A. A. de, Castilho, M. S., Nascimento, P. G., Archanjo, F. C., del Ponte, G., Oliva, G. & Pupo, M. T. (2004). *Bioorg. Med. Chem.* **12**, 4823–4833.
Maruyama, W., Akao, Y., Youdim, M. B., Davis, B. A. & Naoi, M. (2001). *J. Neurochem.* **78**, 727–735.
Matthews, B. W. (1968). *J. Mol. Biol.* **33**, 491–497.
Menezes, I. R., Lopes, J. C., Montanari, C. A., Oliva, G., Pavao, F., Castilho, M. S., Vieira, P. C. & Pupo, M. T. (2003). *J. Comput.-Aided Mol. Des.* **17**, 277–290.
Mercer, W. D., Winn, S. I. & Watson, H. C. (1976). *J. Mol. Biol.* **104**, 277–283.
Morris, G. M., Goodsell, D. S., Huey, R. & Olson, A. J. (1996). *J. Comput.-Aided Mol. Des.* **10**, 293–304.
Morris, R. J., Perrakis, A. & Lamzin, V. S. (2002). *Acta Cryst.* D**58**, 968–975.
Navaza, J. (2001). *Acta Cryst.* D**57**, 1367–1372.
Otwinowski, Z. & Minor, W. (1997). *Methods Enzymol.* **276**, 307–326.
Polekhina, G., House, C. M., Traficante, N., Mackay, J. P., Relaix, F., Sassoon, D. A., Parker, M. W. & Bowtell, D. D. (2002). *Nature Struct. Biol.* **9**, 68–75.
Potterton, E., Briggs, P., Turkenburg, M. & Dodson, E. (2003). *Acta Cryst.* D**59**, 1131–1137.
Roitel, O., Vachette, P., Azza, S. & Branlant, G. (2003). *J. Mol. Biol.* **326**, 1513–1522.
Rossmann, M. G., Moras, D. & Olsen, K. W. (1974). *Nature (London)*, **250**, 194–199.
Sali, A. & Blundell, T. L. (1990). *J. Mol. Biol.* **212**, 403–428.
Satchell, J. F., Malby, R. L., Luo, C. S., Adisa, A., Alpyurek, A. E., Klonis, N., Smith, B. J., Tilley, L. & Colman, P. M. (2005). *Acta Cryst.* D**61**, 1213–1221.
Saunders, P. A., Chen, R. W. & Chuang, D. M. (1999). *J. Neurochem.* **72**, 925–932.
Shen, Y. Q., Li, J., Song, S. Y. & Lin, Z. J. (2000). *J. Struct. Biol.* **130**, 1–9.
Shen, Y. Q., Song, S. Y. & Lin, Z. J. (2002). *Acta Cryst.* D**58**, 1287–1297.
Sherman, I. W. (1998). Editor. *Malaria: Parasite Biology, Pathogenesis and Protection*. Washington, DC: ASM Press.
Shindyalov, I. N. & Bourne, P. E. (1998). *Protein Eng.* **11**, 739–747.
Sirover, M. A. (1996). *Life Sci.* **58**, 2271–2277.
Sirover, M. A. (1997). *J. Cell. Biochem.* **66**, 133–140.
Sirover, M. A. (1999). *Biochim. Biophys. Acta*, **1432**, 159–184.
Skarzynski, T. & Wonacot, A. J. (1988). *J. Mol. Biol.* **203**, 1097–1118.
Sobolev, V., Sorokine, A., Prilusky, J., Abola, E. E. & Edelman, M. (1999). *Bioinformatics*, **15**, 327–332.
Suresh, S., Bressi, J. C., Kennedy, K. J., Verlinde, C. L., Gelb, M. H. & Hol, W. G. (2001). *J. Mol. Biol.* **309**, 423–435.
Talfournier, F., Colloc'h, N., Mornon, J. P. & Branlant, G. (1999). *Eur. J. Biochem.* **265**, 93–104.
Tanner, J. J., Hecht, R. M. & Krause, K. L. (1996). *Biochemistry*, **35**, 2597–2609.
Tatton, W. G., Chalmers-Redman, R., Brown, D. & Tatton, N. (2003). *Ann. Neurol.* **53**, *Suppl.* 3, S61–S72.
Tatton, W., Chalmers-Redman, R. & Tatton, N. (2003). *J. Neural. Transm.* **110**, 509–515.
Van Calenbergh, S., Verlinde, C. L., Soenens, J., De Bruyn, A., Callens, M., Blaton, N. M., Peeters, O. M., Rozenski, J., Hol, W. G. & Herdewijn, P. (1995). *J. Med. Chem.* **38**, 3838–3849.
Vellieux, F. M. D., Hajdu, J., Verlinde, C. L. M. J., Groendijk, H., Read, R. J., Greenhough, T. J., Campbell, J. W., Kalk, K. H., Littlechild, J. A., Watson, H. C. & Hol, W. G. J. (1993). *Proc. Natl Acad. Sci. USA*, **90**, 2355–2359.
Verlinde, C. L., Callens, M., Van Calenbergh, S., Van Aerschot, A., Herdewijn, P., Hannaert, V., Michels, P. A., Opperdoes, F. R. & Hol, W. G. (1994). *J. Med. Chem.* **37**, 3605–3613.
Vollberg, T. M., Siegler, K. M., Cool, B. L. & Sirover, M. A. (1989). *Proc. Natl Acad. Sci. USA*, **86**, 8693–8697.
Warizaya, M., Kinoshita, T., Kato, A., Nakajima, H. & Fujii, T. (2004). *Acta Cryst.* D**60**, 567–568.
Yun, M., Park, C. G., Kim, J. Y. & Park, H. W. (2000). *Biochemistry*, **39**, 10702–10710.